

# Synthetic aperture microscopy based on referenceless phase retrieval with an electrically tunable lens

DENNIS J. LEE,<sup>1,\*</sup> KYUNGHUN HAN,<sup>1,2</sup> HYEON JEONG LEE,<sup>3</sup> AND ANDREW M. WEINER<sup>1,2</sup>

<sup>1</sup>School of Electrical and Computer Engineering, Purdue University, 465 Northwestern Avenue, West Lafayette, Indiana 47907, USA

<sup>2</sup>Birk Nanotechnology Center, Purdue University, 1205 West State Street, West Lafayette, Indiana 47907, USA

<sup>3</sup>Weldon School of Biomedical Engineering, Purdue University, 206 S. Martin Jischke Drive, West Lafayette, Indiana 47907, USA

\*Corresponding author: dennis.lee.1600@gmail.com

Received 6 April 2015; accepted 8 May 2015; posted 11 May 2015 (Doc. ID 237599); published 4 June 2015

Phase imaging microscopy, based either on holography or nonholographic methods such as phase retrieval, has seen considerable attention recently. Phase retrieval offers the advantage of being free of a reference arm and enables a more stable and compact setup. We present an optical setup that provides enhanced resolution by implementing synthetic aperture imaging based on phase retrieval using an electrically tunable lens (ETL). The ETL is a more compact and less expensive alternative to computerized translation stages and spatial light modulators. Before applying phase retrieval, we discuss a general calibration algorithm, which performs image registration, corrects for magnifications, and determines the axial locations of image planes. Finally, we obtain resolution-enhanced images of a phase grating and of cells to demonstrate the practical application of our technique. © 2015 Optical Society of America

**OCIS codes:** (170.0180) Microscopy; (110.1758) Computational imaging; (170.0110) Imaging systems; (100.3010) Image reconstruction techniques; (100.5070) Phase retrieval.

<http://dx.doi.org/10.1364/AO.54.005346>

## 1. INTRODUCTION

Imaging phase objects, such as transparent biological specimens, is an important application in microscopy. A common way to view transparent samples is to use fluorescence. Well-known methods include confocal,  $4\pi$ , structured illumination, and stimulated emission depletion microscopy [1–3]. A drawback is that some samples may not be fluorescent or are not easily fluorescently tagged. Phase objects have an important property in that they induce phase shifts as light diffracts through them. By converting these phase shifts to intensity variations, techniques such as phase contrast or differential interference contrast can qualitatively image phase, which acts as a label-free contrast agent [4–6]. More recent efforts to quantify phase offer the advantage of measuring cell thickness [7], quantifying path lengths [8,9], numerically focusing samples [10–12], and viewing 3D cellular structure [13]. Holography is a commonly used technique to measure phase, but it requires a reference arm, which makes it sensitive to vibrations and temperature changes. Referenceless single beam techniques compute phase from a sequence of diffraction patterns. Some examples of diffraction patterns include defocused images [14–16], spatially modulated illumination [17,18], angular illumination [19], and structured illumination [20,21]. Defocusing images is attractive because it

can be simply implemented by moving a camera on a translation stage [22], applying a lens function on a 2D spatial light modulator (SLM) [23,24], or changing the focal length of an electrically tunable lens (ETL) [25–28]. Of these different ways to defocus, the ETL is a compact, relatively inexpensive option that is free of mechanical motion, in contrast to computerized translation stages or 2D SLMs.

The resolution of phase objects can be improved using different techniques. Some holographic techniques include off-axis illumination [29,30], structured illumination [20,31], or shorter wavelength sources [32]. Synthetic aperture imaging uses off-axis illumination to capture higher spatial frequencies that would be cut off by the finite aperture of the objective lens. For example, electric field images can be captured at different angles based on phase-shifting interferometry [30]. Alternatively, nonholographic techniques can be based on referenceless phase retrieval, which has the advantage of being a more stable and compact setup without requiring expensive components such as a high-frame-rate camera. Some examples of nonholographic methods are based on synthetic aperture imaging [33], structured illumination [34], and angular illumination [19]. The synthetic aperture technique in our earlier work [33] relies on moving a camera via a translation stage for defocus.

In this work, we propose a variant on synthetic aperture microscopy based on referenceless phase retrieval. The proposed method uses an ETL to defocus images, which eliminates the mechanical motion of the translation stage and avoids the cost and bulkiness of a spatial light modulator. As part of this approach, we develop a calibration algorithm to register images, correct for image magnifications, and compute the axial locations of image planes. This algorithm more generally applies to other experiments, which require precise alignment of images or image magnification to be controlled. For example, transport-of-intensity phase microscopy with an ETL [28] and 3D light-sheet microscopy with a tunable lens [26] are sensitive to image alignment and magnification and could benefit from this algorithm.

## 2. EXPERIMENT DESCRIPTION

### A. Setup

Figure 1(a) illustrates the experimental setup. Mirror M1 tilts to scan the sample at different angles. After traveling through the objective lens, light passes through the ETL (Optotune, EL-10-30-C-VIS-LD-MV) with variable focal length controlled by a user-supplied input current. The focal length can be tuned from  $-600$  mm to negative infinity and positive infinity to  $170$  mm over a current range from  $0$  to  $300$  mA [35]. In this nontelecentric configuration, image magnification varies with ETL focal length  $f_{\text{ETL}}$ . In theory, for thin lenses, the magnification factor  $\gamma$ , which results in a scaled image  $I(\gamma x, \gamma y)$ , depends on  $f_{\text{ETL}}$  as

$$\gamma = \frac{f_{\text{ETL}} f_{\text{TL}}}{f_{\text{OL}}(f_{\text{ETL}} + f_{\text{TL}} - d_{\text{ETL/TL}})}, \quad (1)$$

where  $f_{\text{TL}}$  and  $f_{\text{OL}}$  are focal lengths of the tube and objective

lenses, and  $d_{\text{ETL/TL}}$  is the distance between the ETL and TL [36]. Similarly, we can make a theoretical calculation of the axial location  $z$  of an image plane for a given  $f_{\text{ETL}}$ . Note that  $z$  refers to the distance between the sample plane and the plane, which would be imaged onto the CCD for a given  $f_{\text{ETL}}$ . In Fig. 1(c), the sample is located at  $z = 0$ . An image taken at  $z = 0$  refers to the sample imaged onto the CCD; the sample is in focus. In theory,  $z$  depends on  $f_{\text{ETL}}$  as [36]

$$z = \frac{f_{\text{TL}}(d_{\text{ETL/TL}} - f_{\text{ETL}})}{\gamma(d_{\text{ETL/TL}} - (f_{\text{ETL}} + f_{\text{TL}}))} = \frac{f_{\text{OL}}(f_{\text{ETL}} - d_{\text{ETL/TL}})}{f_{\text{ETL}}}. \quad (2)$$

However, the calculations in Eqs. (1) and (2) require precise knowledge of physical parameters such as  $d_{\text{ETL/TL}}$  and  $f_{\text{ETL}}$ . Rather than trying to make precise measurements, we describe a practical algorithm to determine  $\gamma$  and  $z$ .

### B. Overview of the Calibration Algorithm

Next, we describe a calibration algorithm that will correct for image magnifications arising from nontelecentricity, as well as register images and determine the axial locations of image planes. The algorithm sequentially optimizes over these unknown parameters. We note that this sequential strategy is inspired by the algorithm in [24]. As an input to the calibration routine, we measure the complex electric field at the focal plane of the OL [ $z = 0$  in Fig. 1(c)] over all angles to be scanned. We can make this measurement using off-axis interferometry with Fourier filtering [8,9]. After calibration, extra components required for the interferometer can be removed.

In this work, we measure five total angles: one at DC [ $\theta = 0^\circ$  in Fig. 1(c)] plus four angles around the periphery of the back focal plane of the condenser lens [Fig. 1(b)], spaced by  $90^\circ$  and scanned in an approximate circle so that the largest illumination angle is  $\theta = 12.7^\circ$ . Of course, this technique can include more angles. Let us denote the fields measured in the calibration step as  $u_0^c(x, y), \dots, u_4^c(x, y)$ . For example,  $u_0^c(x, y)$  is the field at DC illumination, while  $u_1^c(x, y)$  corresponds to the field measured when the beam is at position 1 [Fig. 1(b)] at the BFP [Fig. 1(a)].

For a given angle of illumination or beam position  $k$  at the BFP, the algorithm begins by numerically propagating the complex electric field  $u_k^c(x, y)$  to different  $z$  planes, where the user supplies an initial guess of the axial locations in sample space. Let  $\hat{z}_1, \dots, \hat{z}_{N_{\text{im}}}$  denote the current guess of the axial locations, where  $N_{\text{im}}$  is the total number of images for a given angle;  $z$  refers to the distance between the sample plane and the plane that would be imaged onto the CCD for a given ETL setting. Let us represent the true axial locations as  $z_1, \dots, z_{N_{\text{im}}}$ . In our experiment, we measure 11 images for each angle ( $N_{\text{im}} = 11$ ), with each image corresponding to a different focal length of the ETL. Note that changing the ETL focal length equivalently defocuses the sample to a different  $z$  [Fig. 1(c)]. After numerical propagation, we obtain a set of simulated images  $\{I_s(x, y; \hat{z}_i): i = 1, \dots, N_{\text{im}}\}$ . Our goal is to match the set of simulated images  $\{I_s(x, y; \hat{z}_i): i = 1, \dots, N_{\text{im}}\}$  with the set of measured images  $\{I_m(x, y; z_i): i = 1, \dots, N_{\text{im}}\}$ . During calibration, we will refine our guess of  $\hat{z}_i$ .

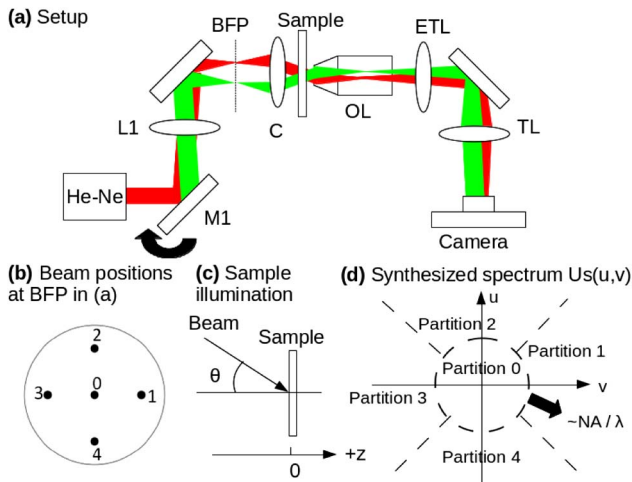


**Fig. 1.** (a) Setup. The red and green rays trace two angles of illumination. He-Ne, 633 nm; M1, gimbal mount mirror; L1, lens ( $f = 300$  mm); BFP, back focal plane of the condenser lens; C, condenser lens; OL, objective lens ( $50\times$ , NA 0.75); ETL, electrically tunable lens; TL, tube lens ( $f = 200$  mm). (c)  $\theta$  is the angle of illumination. (d) We divide  $U_s(u, v)$  into partitions. In partition  $k$ , we set  $U_s(u, v) = U_k(u, v)$ , where  $k$  is the beam position at the BFP in (b), and  $U_k(u, v)$  is the corresponding spectrum.

### C. Strategy for Algorithm Convergence

When trying to match two images, the algorithm may get stuck in a local minimum. The best way to avoid a local minimum is to start with an initial guess that matches the two images as closely as possible. Then the job of the algorithm is to refine the initial guess to optimize the cross-correlation  $\rho$ :

$$\rho = \frac{1}{N} \sum_{x,y} \frac{(I_m(x, y; z_i) - \bar{I}_m)(I_s(x, y; \hat{z}_i) - \bar{I}_s)}{\sigma_m \sigma_s}, \quad (3)$$

where  $\bar{I}_m$  and  $\bar{I}_s$  denote average intensities,  $\sigma_m$  and  $\sigma_s$  are intensity standard deviations for the measured and simulated images, respectively, and  $N$  is the total number of pixels. Cross correlation works best on objects with information-rich features such as clear patterns. We find that we can make a good initial guess by assuming that the image shifts, magnifications, and defocus are linearly proportional to the applied current on the ETL,  $i_{\text{ETL}}$ .

The physical intuition is that as the ETL focal length changes, the lens deforms to different shapes, causing the beam to deflect. For example, suppose a deflection of  $\delta x$  results in a shifted image  $I(x + \delta x, y)$ . As a rough geometrical approximation, we can estimate the shift amount  $\delta x$  to be proportional to  $i_{\text{ETL}}$ ,  $f_{\text{TL}}$ , and the angle of illumination  $\theta$ :

$$\delta x \propto i_{\text{ETL}} f_{\text{TL}} \tan \theta, \quad (4)$$

where  $\theta$  can be measured in a calibration step using off-axis interferometry.

Similarly, given a magnified image  $I(\gamma x, \gamma y)$ , we can roughly predict image magnification  $\gamma$  as a linear function of  $i_{\text{ETL}}$ . In theory, Eq. (1) describes  $\gamma$  as a function of physical parameters. For an initial guess, we start with the simplest relation that  $\gamma$  is linearly proportional to  $i_{\text{ETL}}$ :

$$\gamma \propto i_{\text{ETL}}. \quad (5)$$

To make an initial guess for the axial location of an image plane, suppose an image is located at  $z$ , which we represent as  $I(x, y; z)$ . In theory, Eq. (2) computes  $z$  in terms of physical parameters. Since measuring these parameters is difficult, instead we start with the simplest possible model that  $z$  is proportional to  $i_{\text{ETL}}$ :

$$z \propto i_{\text{ETL}}. \quad (6)$$

One way to make the guesses in Eqs. (4)–(6) more precise is to initially determine  $\delta x$ ,  $\gamma$ , and  $z$  by rough inspection, as  $i_{\text{ETL}}$  varies. Experimentally, we find that this strategy brings these parameters close enough to the actual values, so that the calibration algorithm, described below, can compute the correct values.

### D. Registering Images

According to the pixel size  $\delta_p$  of the sensor array, the intensities  $I(x, y)$  are sampled as  $I[m, n] = I(m\delta_p, n\delta_p)$ . The sampled simulated and measured images can be represented as

$$I_s[m, n; \hat{z}_i] = I_s(m\delta_p, n\delta_p; \hat{z}_i) \quad (7)$$

and

$$I_m[m, n; z_i] = I_m(m\delta_p, n\delta_p; z_i). \quad (8)$$

The next step in the calibration algorithm is to shift the measured images in the horizontal and vertical directions to optimally match the simulated intensity images by maximizing  $\rho_1$ :

$$\rho_1(\Delta_m, \Delta_n) = \frac{1}{N} \sum_{m,n} \frac{(I_m[m + \Delta_m, n + \Delta_n; z_i] - \bar{I}_m)(I_s[m, n; \hat{z}_i] - \bar{I}_s)}{\sigma_m \sigma_s}, \quad (9)$$

where  $\Delta_m$  and  $\Delta_n$  are the pixel shift amounts to be tested. We find that trying values  $-11 \leq \Delta_m, \Delta_n \leq 11$  gives good, convergent results. Once we find the optimal shifts  $\Delta_m^*$  and  $\Delta_n^*$ , as

$$(\Delta_m^*, \Delta_n^*) = \underset{\Delta_m, \Delta_n}{\operatorname{argmax}} \rho_1(\Delta_m, \Delta_n), \quad (10)$$

we update the measured image as

$$I_m[m, n; z_i] \leftarrow I_m[m + \Delta_m^*, n + \Delta_n^*; z_i]. \quad (11)$$

### E. Rescaling Images

Next, we would like to find the magnification  $\gamma$  that maximizes the cross-correlation  $\rho_2$ :

$$\rho_2(\gamma) = \frac{1}{N} \sum_{m,n} \frac{(I_m[\gamma m, \gamma n; z_i] - \bar{I}_m)(I_s[m, n; \hat{z}_i] - \bar{I}_s)}{\sigma_m \sigma_s}. \quad (12)$$

The general strategy is to try different values for  $\gamma$  and find the optimal  $\gamma^*$  that maximizes  $\rho_2$ . Since  $\gamma m$  or  $\gamma n$  may not be integer-valued, the magnified image  $I_m[\gamma m, \gamma n; z_i]$  can be computed using bicubic interpolation. We find that trying values in the range  $0.99 \leq \gamma \leq 1.01$ , sampled in increments of 0.002, yields convergent results. We compute the optimal  $\gamma^*$  as

$$\gamma^* = \underset{\gamma}{\operatorname{argmax}} \rho_2(\gamma) \quad (13)$$

and update the measured image with the optimal  $\gamma^*$ :

$$I_m[m, n; z_i] \leftarrow I_m[\gamma^* m, \gamma^* n; z_i]. \quad (14)$$

### F. Calculating Axial Locations of Image Planes

Next, we would like to find the amount of defocus  $\Delta_z$  that maximizes the cross-correlation  $\rho_3$ :

$$\rho_3(\Delta_z) = \frac{1}{N} \sum_{m,n} \frac{(I_m[m, n; z_i] - \bar{I}_m)(I_s[m, n; \hat{z}_i + \Delta_z] - \bar{I}_s)}{\sigma_m \sigma_s}. \quad (15)$$

Using a similar strategy as before, we test different values of  $\Delta_z$  in the range  $-1 \mu\text{m} \leq \Delta_z \leq 1 \mu\text{m}$ , sampled in increments of  $0.1 \mu\text{m}$ . We find that trying these values yields a convergent algorithm. For each value of  $\Delta_z$ , we simulate propagation of the complex electric field  $u_k^c(x, y)$  to  $\hat{z}_i + \Delta_z$ , measured in the calibration step, as described in Section B. We compute the optimal  $\Delta_z^*$  as

$$\Delta_z^* = \underset{\Delta_z}{\operatorname{argmax}} \rho_3(\Delta_z). \quad (16)$$

Then, we update the axial location  $\hat{z}_i$  of image plane  $i$  with the optimal value  $\Delta_z^*$ :

$$\hat{z}_i \leftarrow \hat{z}_i + \Delta_z^*, \quad (17)$$

and the simulated image is updated with the optimal value  $\Delta_z^*$ :

$$I_s[m, n; \hat{z}_i] \leftarrow I_s[m, n; \hat{z}_i + \Delta_z^*]. \quad (18)$$

After this update, the algorithm loops to repeat the steps of registering and rescaling images and optimizing image axial locations until there is no change in the parameters. In other words, for each image, the calibration loop terminates when  $\Delta_m^* \Delta_n^* = 0$ ,  $\gamma^* = 1$ , and  $\Delta_z^* = 0$ . Figure 2 summarizes this procedure in a top-level flow chart.

### G. Calibration Example

To illustrate the action of the calibration program, we examine a phase grating sample. The sample consists of gratings with different periods patterned in PMMA film ( $n = 1.49$ ) on a glass substrate. For calibration, we examine a portion of the sample with a 12  $\mu\text{m}$  grating and display measured images before and after calibration, as well as simulated (numerically propagated) images after calibration, in Figs. 3(a) to 3(c). We see that the shifts and magnifications have been corrected, so

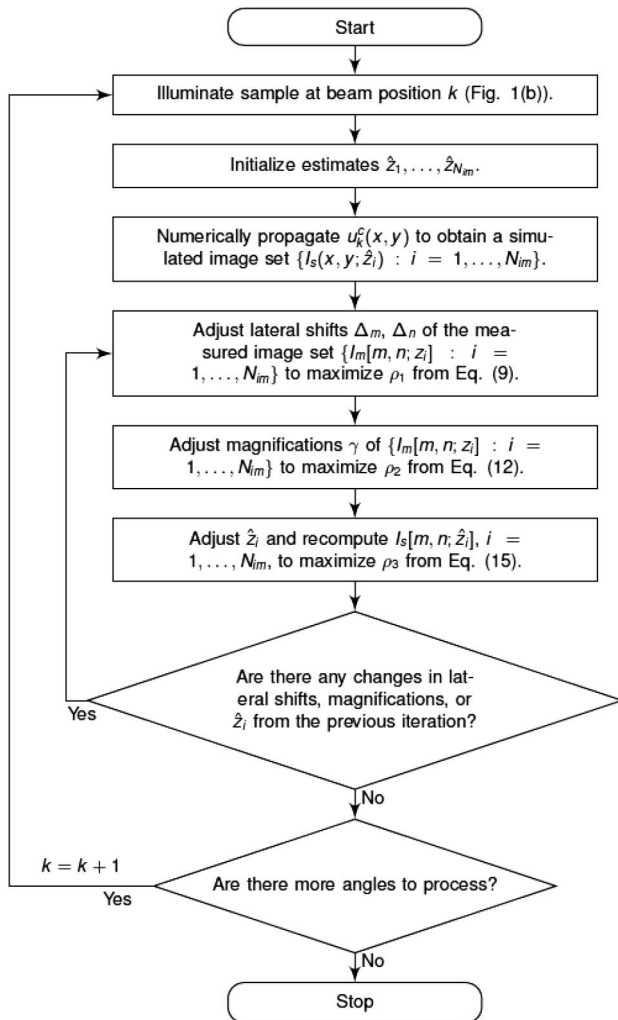


**Fig. 2.** Flow chart of the calibration algorithm. The program performs image registration, corrects for magnifications, and determines the axial locations of image planes.

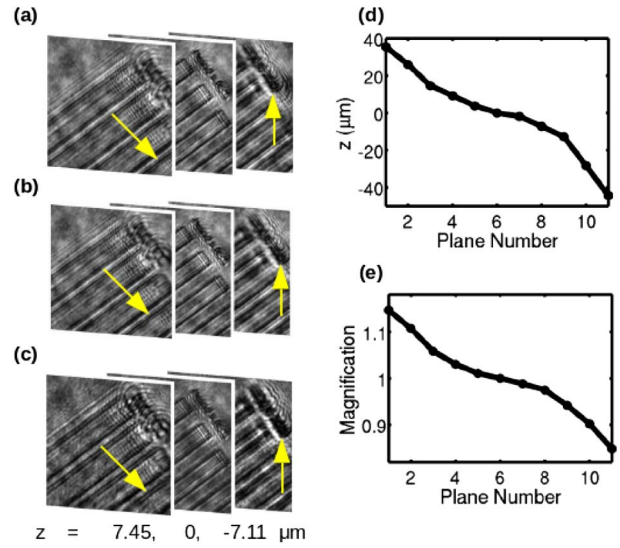


**Fig. 3.** Images of a 12  $\mu\text{m}$  period grating with  $\theta = 12.7^\circ$ , before and after calibration. Note the measured and simulated images agree after calibration in (b) and (c). The yellow arrows highlight shifts, which have been corrected. (a) Measured images, before calibration. (b) Measured images, after calibration. (c) Simulated images, after calibration. (d) Defocus amount  $z$ . (e) Magnification.

that the measured and simulated images agree in Figs. 3(b) and 3(c).

To retrieve phase, we need to know how much each image is defocused along the  $z$  axis. Figures 3(d) and 3(e) plot the axial locations and magnifications for DC illumination, values typical over all angles. We designate the middle plane (plane 6) to be the focal plane ( $z = 0$ ). By design, we choose the plane spacing to increase nonlinearly (approximately exponentially) in relation to the focal plane. We use the approximation that the amount of defocus is linearly related to the change in current applied to the ETL. The more closely spaced images capture high-frequency variations in intensity, while images with more defocus contain low-frequency information [37]. These images are constraints for an iterative phase-retrieval algorithm [15]. At each axial location, we compute an electric field with magnitude based on camera measurements and phase based on numerical propagation from the previous plane. This computation is iteratively repeated over each axial location to produce a phase that is consistent with our measurements [16].

After retrieving the phase for each angle of illumination, we combine the resulting complex electric fields (synthetic aperture imaging). Each field at oblique illumination highlights a portion of the spatial frequency domain not accessible by the DC field alone. We construct a synthesized spectrum  $U_s(u, v)$  by first assigning the low frequencies (of radius approximately  $NA/\lambda$ ) to be equal to the DC spectrum, denoted as  $U_0(u, v)$ . In other words, in partition 0 [Fig. 1(d)],  $U_s(u, v) = U_0(u, v)$ . When the beam is positioned at the periphery of the BFP [numbered as 1, ..., 4 in Fig. 1(b)], let us denote the Fourier transform of the fields measured at these angles as  $U_1(u, v), \dots, U_4(u, v)$ . Next, we assign other partitions of  $U_s(u, v)$  to corresponding spectra. For example, in partition 1 [Fig. 1(d)],  $U_s(u, v) = U_1(u, v)$ . Taking the inverse Fourier

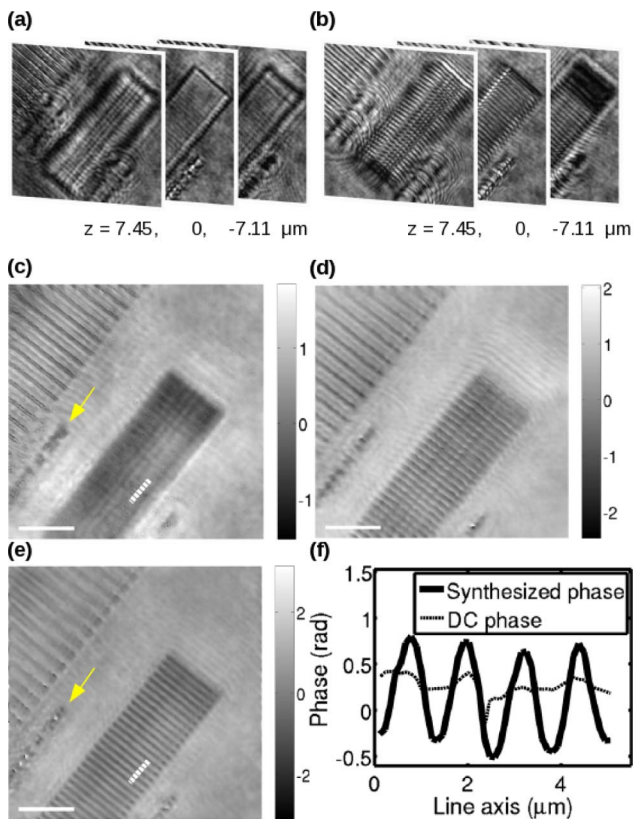
transform of  $U_s(u, v)$ , we can extract the synthesized phase [33].

### 3. RESULTS

#### A. Phase Reconstruction of a 1 $\mu\text{m}$ Grating

To demonstrate resolution enhancement, we first image a phase grating sample with a 1  $\mu\text{m}$  period. In an earlier step (Fig. 3), we have determined the calibration parameters (lateral shifts, magnifications, and axial locations) by examining a different portion of the sample. The grating is patterned in PMMA film by electron beam lithography. Since the grating grooves lie below the planar surface of the PMMA film, we expect the grooves to have a shorter path length and, hence, appear darker than the background. The film thickness of 1.5  $\mu\text{m}$  corresponds to a phase shift of  $(2\pi/\lambda)\Delta n\Delta z - 2\pi \approx 1$  rad, where  $\Delta n = 1.49 - 1 = 0.49$ ,  $\Delta z = 1.5$   $\mu\text{m}$ ,  $\lambda = 633$  nm, and we account for phase wrapping by subtracting  $2\pi$ .

Figures 4(a) and 4(c) show some measured intensity images and the DC phase, respectively, in which the 1  $\mu\text{m}$  grating pattern is indiscernible. Under oblique illumination, the higher-frequency pattern pops into view in Figs. 4(b) and 4(d) as a vivid demonstration of previously inaccessible frequency content. These angular fields enhance the resulting synthesized phase, so that the pattern becomes clearly distinguishable in



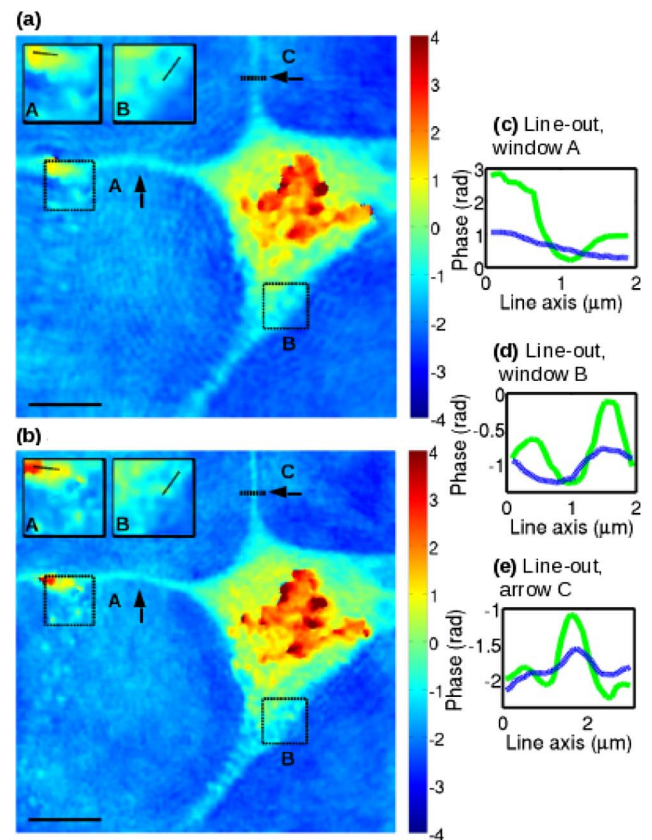
**Fig. 4.** Phase reconstruction of a grating sample with a 1  $\mu\text{m}$  period (center grating). (a) Intensity images,  $\theta = 0^\circ$ , (b) intensity images,  $\theta = 12.7^\circ$ , (c) DC phase image,  $\theta = 0^\circ$ , (d) phase image,  $\theta = 12.7^\circ$ , (e) synthesized phase image, and (f) line-outs from (c) and (e). (c) and (e) Yellow arrows highlight focusing dots, which become more sharpened in (e). Scale bars: 8  $\mu\text{m}$ .

Fig. 4(e) and in the line-outs [Fig. 4(f)]. The modulation depth of the grating in Fig. 4(f), measured by averaging the peak-to-valley heights in the synthesized phase line-out, is about 1 rad, which matches the expected phase shift given the PMMA film thickness of 1.5  $\mu\text{m}$ .

#### B. Phase Reconstruction of a Biological Cell

Next, we apply our technique to imaging cells, an important practical application. Fixed unstained cells from the human embryonic kidney 293 (HEK-293) line serve as our sample of interest. For calibration, we examine a portion of the sample to correct for the lateral shifts. The magnifications and axial locations should be the same as determined from the phase grating. The lateral shifts differ because the beam travels through different material: PMMA film on glass substrate in one case, and a glass slide and phosphate buffered saline (PBS) medium in the other case. Once obtained, the calibration parameters apply to other samples made of the same materials.

A neuron-like cell from this sample, shown in Fig. 5(a), exhibits interesting phase features such as dendrites (labeled with arrows) and cellular structure, which we hope to better resolve. Using retrieved phases from multiple illumination angles, we construct the synthesized spectrum according to Fig. 1(d). The resulting synthesized phase displays features enhanced in resolution. To aid visualization, boxes A and B in Figs. 5(a) and 5(b) highlight phase enhancements with the corresponding line-outs plotted in Figs. 5(c) and 5(d). In particular, an axon



**Fig. 5.** Phase reconstruction of a HEK-293 cell. (a) DC phase and (b) synthesized phase. (c)–(e) Green line: synthesized phase, blue line: DC phase. Scale bars: 8  $\mu\text{m}$ .

terminal becomes more visible in box A. Additionally, the dendrites, labeled with arrows, show more clearly defined profiles in the synthesized phase.

To quantify the resolution improvement, we can first estimate the resolution before synthetic aperture imaging. In window B, we see an example of two features, which are barely resolvable in the DC phase but become distinguishable in the synthesized phase, as indicated by the line-out in Fig. 5(d). We estimate that these two features are separated by 1.2  $\mu\text{m}$ , based on the green line (synthesized phase) in the line-out. Hence,

$$\delta = \frac{\kappa\lambda}{\text{NA}} = 1.2 \mu\text{m}, \quad (19)$$

where  $\kappa$  is an experimental parameter that depends on factors like the signal-to-noise ratio of the detector,  $\lambda = 633 \text{ nm}$ , and  $\text{NA} = 0.75$ . After synthetic aperture imaging, NA improves to  $\text{NA} + \sin \theta_{\text{illum}} = 0.97$ , and the resolution improves to

$$\delta = \frac{\kappa\lambda}{\text{NA} + \sin \theta_{\text{illum}}} = 0.9 \mu\text{m}, \quad (20)$$

where  $\theta_{\text{illum}} = 12.7^\circ$  is the largest angle of illumination used in our experiment. This value makes sense, since we are able to resolve the 1  $\mu\text{m}$  grating in the synthesized phase, as shown by the line-out in Fig. 4(f).

#### 4. CONCLUSION

We have demonstrated synthetic aperture microscopy based on referenceless phase retrieval with an electrically tunable lens. The ETL is a compact, relatively low-cost device, in contrast to other defocusing mechanisms such as a moving translation stage or 2D SLM. We have devised a calibration algorithm to register and rescale images and compute the axial locations of image planes. The developed algorithm is more generally useful for applications that are sensitive to image alignment, scaling, or defocus, and it may enable other applications to benefit from the use of an ETL.

National Science Foundation (NSF) (ECCS-1102110).

We gratefully acknowledge Prof. Minghao Qi for advice on fabricating the grating sample and Prof. Ji-Xin Cheng for discussing cell preparation. We thank Prof. Juliet Gopinath and Ramzi Zahreddine for detailed conversations about the ETL.

#### REFERENCES

- M. G. L. Gustafsson, "Nonlinear structured-illumination microscopy: wide-field fluorescence imaging with theoretically unlimited resolution," *Proc. Natl. Acad. Sci. USA* **102**, 13081 (2005).
- S. W. Hell and J. Wichmann, "Breaking the diffraction resolution limit by stimulated emission: stimulated-emission-depletion fluorescence microscopy," *Opt. Lett.* **19**, 780–782 (1994).
- B. Huang, M. Bates, and X. Zhuang, "Super-resolution fluorescence microscopy," *Annu. Rev. Biochem.* **78**, 993–1016 (2009).
- D. J. Stephens and V. J. Allan, "Light microscopy techniques for live cell imaging," *Science* **300**, 82–86 (2003).
- D. B. Murphy, *Fundamentals of Light Microscopy and Electronic Imaging* (Wiley-Liss, 2001).
- F. Zernike, "Phase contrast, a new method for microscopic observation of transparent objects," *Physica* **9**, 686–698 and 975–986 (1942).
- G. Popescu, T. Ikeda, R. R. Dasari, and M. S. Feld, "Diffraction phase microscopy for quantifying cell structure and dynamics," *Opt. Lett.* **31**, 775–777 (2006).
- E. Cuche, P. Marquet, and C. Depeursinge, "Simultaneous amplitude-contrast and quantitative phase-contrast microscopy by numerical reconstruction of Fresnel off-axis holograms," *Appl. Opt.* **38**, 6994–7001 (1999).
- E. Cuche, P. Marquet, and C. Depeursinge, "Spatial filtering for zero-order and twin-image elimination in digital off-axis holography," *Appl. Opt.* **39**, 4070–4075 (2000).
- U. Schnars and W. Juptner, "Direct recording of holograms by a CCD target and numerical reconstruction," *Appl. Opt.* **33**, 179–181 (1994).
- I. Yamaguchi and T. Zhang, "Phase-shifting digital holography," *Opt. Lett.* **22**, 1268–1270 (1997).
- J. Goodman, *Introduction to Fourier Optics*, 3rd ed. (Roberts & Company, 2005).
- W. Choi, C. Fang-Yen, K. Badizadegan, S. Oh, N. Lue, R. R. Dasari, and M. S. Feld, "Tomographic phase microscopy," *Nat. Methods* **4**, 717–719 (2007).
- L. Allen and M. Oxley, "Phase retrieval from series of images obtained by defocus variation," *Opt. Commun.* **199**, 65–75 (2001).
- J. R. Fienup, "Phase retrieval algorithms: a comparison," *Appl. Opt.* **21**, 2758–2769 (1982).
- G. Pedrini, W. Osten, and H. Tiziani, "Wave-front reconstruction from a sequence of interferograms recorded at different planes," *Opt. Lett.* **30**, 833–835 (2005).
- P. Gao, G. Pedrini, C. Zuo, and W. Osten, "Phase retrieval using spatially modulated illumination," *Opt. Lett.* **39**, 3615–3618 (2014).
- J. A. Rodrigo, T. Alieva, G. Cristóbal, and M. L. Calvo, "Wavefield imaging via iterative retrieval based on phase modulation diversity," *Opt. Express* **19**, 18621–18635 (2011).
- G. Zheng, R. Horstmeyer, and C. Yang, "Wide-field, high-resolution Fourier ptychographic microscopy," *Nat. Photonics* **7**, 739–745 (2013).
- P. Gao, G. Pedrini, and W. Osten, "Structured illumination for resolution enhancement and autofocusing in digital holographic microscopy," *Opt. Lett.* **38**, 1328–1330 (2013).
- F. Zhang, G. Pedrini, and W. Osten, "Phase retrieval of arbitrary complex-valued fields through aperture-plane modulation," *Phys. Rev. A* **75**, 043805 (2007).
- P. Almoró, G. Pedrini, and W. Osten, "Complete wavefront reconstruction using sequential intensity measurements of a volume speckle field," *Appl. Opt.* **45**, 8596–8605 (2006).
- P. F. Almoró, L. Waller, M. Agour, C. Falldorf, G. Pedrini, W. Osten, and S. G. Hanson, "Enhanced deterministic phase retrieval using a partially developed speckle field," *Opt. Lett.* **37**, 2088–2090 (2012).
- L. Camacho, V. Mico, Z. Zalevsky, and J. Garcia, "Quantitative phase microscopy using defocusing by means of a spatial light modulator," *Opt. Express* **18**, 6755–6766 (2010).
- J. M. Jabbour, B. H. Malik, C. Olsovsky, R. Cuenca, S. Cheng, J. A. Jo, Y.-S. Cheng, J. M. Wright, and K. C. Maitland, "Optical axial scanning in confocal microscopy using an electrically tunable lens," *Biomed. Opt. Express* **5**, 645–652 (2014).
- F. O. Fahrbach, F. F. Voigt, B. Schmid, F. Helmchen, and J. Huisken, "Rapid 3D light-sheet microscopy with a tunable lens," *Opt. Express* **21**, 21010–21026 (2013).
- B. F. Grewe, F. F. Voigt, M. Hoff, and F. Helmchen, "Fast two-layer two-photon imaging of neuronal cell populations using an electrically tunable lens," *Biomed. Opt. Express* **2**, 2035–2046 (2011).
- C. Zuo, Q. Chen, W. Qu, and A. Asundi, "High-speed transport-of-intensity phase microscopy with an electrically tunable lens," *Opt. Express* **21**, 24060–24075 (2013).
- S. A. Alexandrov, T. R. Hillman, T. Gutzler, and D. D. Sampson, "Synthetic aperture Fourier holographic optical microscopy," *Phys. Rev. Lett.* **97**, 168102 (2006).
- M. Kim, Y. Choi, C. Fang-Yen, Y. Sung, K. Kim, R. R. Dasari, M. S. Feld, and W. Choi, "Three-dimensional differential interference contrast microscopy using synthetic aperture imaging," *J. Biomed. Opt.* **17**, 026003 (2012).
- S. Chowdhury and J. Izatt, "Structured illumination diffraction phase microscopy for broadband, subdiffraction resolution, quantitative phase imaging," *Opt. Lett.* **39**, 1015–1018 (2014).
- A. Faridian, D. Hopp, G. Pedrini, U. Eigenthaler, M. Hirscher, and W. Osten, "Nanoscale imaging using deep ultraviolet digital holographic microscopy," *Opt. Express* **18**, 14159–14164 (2010).

33. D. J. Lee and A. M. Weiner, "Optical phase imaging using a synthetic aperture phase retrieval technique," *Opt. Express* **22**, 9380–9394 (2014).
34. P. Gao, G. Pedrini, and W. Osten, "Phase retrieval with resolution enhancement by using structured illumination," *Opt. Lett.* **38**, 5204–5207 (2013).
35. Optotune Datasheet, "EL-10-30 Series," (Optotune, 2015), <http://www.optotune.com/images/products/Optotune%20EL-10-30.pdf>.
36. E. Hecht, *Optics*, 4th ed. (Pearson Education, 2002).
37. Z. Jingshan, R. Claus, J. Dauwels, L. Tian, and L. Waller, "Transport of intensity phase imaging by intensity spectrum fitting of exponentially spaced defocus planes," *Opt. Express* **22**, 10661–10674 (2014).